Available online at www.sciencedirect.com
ScienceDirect
Journal of Magnetic Resonance 189 (2007) 46–58
JMR Journal of Magnetic Resonance
www.elsevier.com/locate/jmr

Spectroscopic imaging from spatially-encoded single-scan multidimensional MRI data

Assaf Tal, Lucio Frydman *

Department of Chemical Physics, Weizmann Institute of Science, 76100 Rehovot, Israel

Received 7 June 2007
Available online 11 August 2007

Abstract

We have recently proposed a protocol for retrieving multidimensional magnetic resonance images within a single scan, based on a spatial encoding of the spin interactions. This methodology relies on progressively dephasing spin coherences throughout a sample; for instance, by sweeping a radiofrequency pulse in the presence of a magnetic field gradient. When spins are suitably refocused by a second (acquisition) field gradient, this yields a time-domain signal reflecting in its magnitude the spatial distribution of spins throughout the sample. It is hereby shown that whereas the absolute value of the resulting signals conveys such imaging information, the hitherto unutilized phase modulation of the signal encodes the chemical shift offsets of the present speciae. Spectroscopically-resolved multidimensional images can thereby be retrieved in this fashion at no additional expense in either experimental complexity, sensitivity or acquisition time—simply by performing an additional analysis of the collected data. The resulting approach to single-scan spectroscopic imaging can also incorporate "RF shimming" compensating abilities, capable of providing high-resolution spectral and high-definition imaging data even under the presence of substantial magnetic field inhomogeneities. The principles of these methodologies as applied to spectroscopic imaging are briefly reviewed and compared against the background of traditional Fourier-based single-scan spectroscopic imaging protocols. Demonstrations of these new multidimensional spectroscopic MRI experiments on simple phantoms are also given.

Keywords: Spectroscopic imaging; Ultrafast MRI; Spatial encoding; Inhomogeneity compensation; EPSI

1. Introduction

Nuclear magnetic resonance (NMR) finds its two main areas of application in the fields of chemical analysis, and in the non-invasive spatial visualization of spin densities [1–3]. When operating in an analytical mode NMR affords information about the nature and the quantity of the analytes being scrutinized, according to the peak positions and the intensities appearing in its spectrum [2]. Monitoring these peaks benefits from the highest possible magnetic field homogeneity, which in turn leads to the sharpest line shapes and to an optimal site resolution. By contrast, when operating in a spatial visualization (MRI) mode, it is the spins' positions that are being sought [3]. These are usually mapped into frequencies with the aid of auxiliary field gradients translating the spins' coordinates into offsets in a one-to-one fashion [4,5]; positions are thereby imprinted in the NMR line shapes at the expense of a significant broadening of the resonances. The needs placed by the spectroscopic and imaging modalities imply that extracting both the chemical nature of a spin as well as its position within the sample, is associated with conflicting demands that do not suit a one-dimensional NMR acquisition. On the other hand spectroscopic imaging measurements can be achieved without complications by relying on multidimensional experiments [1–3,6], which separate and correlate what may otherwise be conflicting modes of observation. The resulting experiments are usually characterized by at least one spectral and up to three spatial dimensions [7–10], and their usefulness in *in vivo* investigations has been demonstrated in a number of contexts [11–14].

* Corresponding author. Fax: +972 8 9344123.
E-mail address: lucio.frydman@weizmann.ac.il (L. Frydman).

1090-7807/$ - see front matter
doi:10.1016/j.jmr.2007.08.003

Due to its inherent multidimensional nature, spectroscopic imaging will usually demand relatively longer acquisition time than its one-dimensional NMR counterparts. A variety of ways have consequently been discussed for accelerating this kind of experiments [15,16]. Many of these variants rely on methods stemming from Mansfield's echo-planar imaging (EPI) and echo-planar spectroscopic imaging (EPSI) propositions [17,18]. These are "ultrafast" approaches relying on oscillating the imaging gradients so as to monitor sizable volumes of the hybrid k/t-space within a single scan; applying a Fourier transform (FT) on the resulting signals yields then the desired correlations between the position-derived and the chemical-shift-derived spin precession frequencies. In addition to such strategies derived from "walks" in the k or k/t-spaces [19,20], we have recently discussed alternative approaches to the acquisition of multidimensional NMR data within a single scan that rely on encoding the spins' evolution along an ancillary, spatially-encoded domain [21,22]. The resulting "ultrafast" nD NMR protocol is applicable within a purely spectroscopic and/or an imaging scenario, and it is the latter that constitutes the starting point of the present work. As explained elsewhere in further detail [23] spatially-encoded MRI retrieves a multidimensional image within a single scan, by applying an external magnetic field gradient that spreads out the resonance frequencies, in conjunction with a frequency-incremented excitation or inversion of the spins. This imposes a quadratic phase encoding $\phi_e(r) \approx Cr^2$ on the spins which, when subsequently read out under the presence of an acquisition gradient G_a, results in a signal whose modulus is directly proportional to the spin density $\rho(r)$ of the object in question. Such imaging principle operates without subjecting its data to a FT, and it can be exploited in a number of ways to obtain 2D NMR images within a single scan [24]. When comparing the method's performance against EPI-based schemes, however, the results offer a mixed outcome. On one hand it is clear that EPI schemes make a more efficient use of the available gradient action k, towards the reading out of the images. On the other hand it was shown that the built-in selectivity underlying spatially-encoding provides a route to reduce field inhomogeneity distortions, which may otherwise affect EPI's low-bandwidth dimension.

The present work explores a different aspect related to the application of spatial encoding principles within an imaging scenario, stemming this time from the method's ability to differentiate between various chemical shifts contributing to the image—at no additional expense in the experiment's complexity. It is here demonstrated that in spatially-encoded MRI, the presence of multiple chemical sites will create a modulation of the phases characterizing the read-out signals. Such phase effects were heretofore disregarded, as the image-reconstruction procedure solely involved a magnitude data calculation. Yet it is shown that by applying a simple FT-based processing on the spatially-encoded data, this phase information can be exploited for the sake of retrieving an NMR spectrum as well as its associated spatial distribution, yielding in effect a new approach to single-scan spectroscopic imaging. Performancewise the resulting approach compares favorably with EPSI-type single-scan experiments, even if its scope of applications may be more limited. It is also shown that in this kind of spectroscopic imaging, high-resolution spectroscopic and high-definition MRI acquisitions are still feasible even if spins are subject to sizable distortions of the ideal B_o static magnetic field.

The operation of spatially-encoded ultrafast spectroscopic imaging experiments are illustrated in this work for a number of simplified scenarios. The methodology's principles are first reviewed for unidimensional objects; examples of the method's operation are given, and its relative merits and potential artifacts are briefly assessed. We then describe the method's extension to higher spatial dimensions, with experimental demonstrations and comparisons against EPI results on a simple phantom. Finally, we discuss and demonstrate the method's ability to afford its spectroscopic imaging information even in the presence of field inhomogeneities, both using basic approaches as well as with a new sequence designed to better handle the presence of multiple chemical sites.

2. Single-scan spatially-encoded spectroscopic imaging on one-dimensional objects

2.1. Basic treatment

We address first the simplest application of spatial encoding to spectroscopic imaging, dealing with a sample characterized by a discrete spectral distribution of chemical shifts $I(\Omega)$, each of which possesses a one-dimensional spin-density profile $\rho_\Omega(z)$. Traditional imaging retrieves the spins' spatial distribution by working on-resonance and monitoring the effects of a constant gradient on the signal following a broad-band excitation pulse (Fig. 1a), whereas ultrafast 2D EPSI seeks to correlate the z and Ω distributions by homogeneously exciting the spins, and then monitoring their signals while under the effect of an oscillating

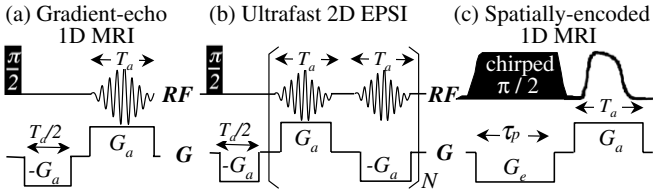

Fig. 1. Imaging and spectroscopic imaging single-scan schemes considered in this study. (a) Conventional gradient-echo k-domain scheme leading to a $\rho(z)$ image after FT. (b) Echo-planar spectroscopic imaging (EPSI) approach leading to shift-resolved $\rho_\Omega(z)$ spatial distributions via the acquisition of multiple (N) gradient-echo signals. (c) Non-FT scheme introduced in Ref. [23] whereby positions initially encoded via a chirped $\pi/2$ pulse acting in the presence of a gradient, are subsequently read out in the time domain by an acquisition gradient. This work demonstrates how 2D $\rho_\Omega(z)$ spectroscopic imaging distributions can also be retrieved from the resulting $S(t)$ signals.

gradient echo train (Fig. 1b). By contrast to these FT-based methods, spatially-encoded imaging relies on preparing the spins with an initial quadratic phase, $\phi_e(z)$. Such profile can be delivered by a sequential excitation based on a linearly-swept radiofrequency pulse, acting while under the action of a constant field gradient G_e (Fig. 1c) [25–28]. With its amplitude suitably tuned, this chirped RF pulse sweeping at a constant rate R between initial and final offset values $O_i = -\gamma G_e L/2$ and $O_f = \gamma G_e L/2$ over a period τ_p (with $-L/2 \leqslant z \leqslant L/2$ defining the field-of-view, FOV), will impart on isochromats a set of position-dependent phases given by

$$\phi_e(z) = \phi_{RF}[\tau(z)] + [\tau_p - \tau(z)] \cdot (\gamma G_e z + \Omega_0). \tag{1}$$

Here

$$\phi_{RF}[\tau(z)] = \int_0^{\tau(z)} [O_i + Rt'] \, dt', \;\; \tau(z) = \frac{\Omega_0 + \gamma G_e z - O_i}{R} \tag{2}$$

denote, respectively, the phase of the RF pulse and the instant $0 \leqslant \tau(z) \leqslant \tau_p$ when the RF addresses a z-dependent isochromat. Replacing these definitions into Eq. (1) leads to

$$\phi_e(z) = \left[-\frac{(\gamma G_e)^2 \tau_p}{2(O_f - O_i)} \right] z^2 + \left[\frac{\gamma G_e \tau_p (O_f - \Omega_0)}{(O_f - O_i)} \right] z^1 + \left[\frac{\tau_p (2 O_f \Omega_0 - O_i^2 - \Omega_0^2)}{2(O_f - O_i)} \right] z^0. \tag{3}$$

This quadratic phase expression is analogous to other literature derivations [23–28], except for the inclusion of a Ω_0 shift term which in imaging is usually taken as zero. The spatially-encoded protocol then delivers its information by monitoring the spins while under the action of a G_a acquisition gradient, driving a wavenumber $k(t) = \gamma \int_0^t G_a(t') \, dt' = \gamma G_a t$. The resulting free induction decay (FID) signal can be written as:

$$S(t) \propto \int_{\text{all } z} \rho_{\Omega_0}(z) \, e^{i \Phi_{\Omega_0}(z,t)} \, dz, \tag{4}$$

where the chemical-shift-dependent $\rho_{\Omega_0}(z)$ spatial profile is modulated by an overall phase

$$\Phi_{\Omega_0}(z,t) = \phi_e(z) + k(t) z + \Omega_0 t \tag{5}$$

depending on the spin's position via $k(t)z$, and on chemical shifts by the usual free evolution term $\Omega_0 t$. Under these conditions the resulting $S(t)$ will reflect, at any given instant, solely those spins located at z_k coordinates that fulfill the stationary phase condition

$$\frac{d}{dz} [\Phi_{\Omega_0}(z,t)]_{z = z_{k(t)}} = 0; \tag{6}$$

this in turn leads to a signal

$$S(t) \propto \Delta z \cdot \rho_{\Omega_0}(z_{k(t)}) \, \exp\left[i \Phi_{\Omega_0}(z_{k(t)}, t) \right]. \tag{7}$$

The Δz term in this expression describes a constant spatial resolution parameter $\sqrt{\frac{FOV}{\gamma G_e \tau_p}}$ that is independent of shift; this and the linear dependence that $z_{k(t)}$ exhibits on k/t, results in an imaging approach whereby spin densities are simply obtained by taking the absolute value of the observed signal: $\rho(z_{k(t)}) \propto |S(t)|$ [23]. Notice that by taking the FID's absolute value this approach, (i) does not make use of the usual numerical FT, and (ii) it disregards the phase information available in the signal. This information could become valuable when considering the presence of multiple chemically-shifted sites. In such instance multiple terms akin to that in Eq. (7) would arise:

$$S(t) \propto \Delta z \cdot \sum_j \rho_{\Omega_j}(z_{k(t)}) \, \exp\left[i \Phi_{\Omega_j}(z_{k(t)}, t) \right]. \tag{8}$$

This sum introduces a site-dependent beat among the profiles, which will distort the image arising upon performing a simple magnitude calculation of the data. Indeed on examining the expressions given so far, one notices that for each individual chemical shift Ω_j the original experiment will be affected in two main ways. At an excitation level chemical shifts will enter the linear term in the excitation phase expression $\phi_e(z)$ (Ω_0-containing term in Eq. (3)); this will shift the overall acquisition path $z_{k(t)}$ of each site by a slight $\frac{\Omega_j}{\gamma G_e}$ displacement, which now becomes

$$z_{k(t)} = \left(\frac{L}{2} - \frac{\Omega_j}{\gamma G_e} \right) - \frac{L}{T_a} \cdot t. \tag{9}$$

Here, we have assumed that a constant acquisition gradient has been applied over a time T_a, chosen so as to unravel the full extent of the initial encoding; i.e., $G_a T_a = -G_e \tau_p$. More significant and relevant for the present treatment than these displacements, are the multiple time-dependent $\Omega_j t$ terms that will now enter in the summation of Eq. (8), owing to the various sites' differing $\Phi_{\Omega_j}(z,t)$ phases. It is these differing contributions that we propose to exploit for extracting chemical shift information out of this imaging-oriented acquisition, transforming it into a spectroscopic imaging experiment.

To find the full Ω_j-dependence that each site will impart on the FID, we consider contributions of only those $z_{k(t)}$ voxels contributing to each site's signal at any particular time. To do so we insert the time-dependence defining each $z_{k(t)}$ in Eq. (9), into z-dependent terms derived for the overall phase in Eq. (5). Ignoring for simplicity all constant-phase factors, this leads to

$$\Phi_{\Omega_0}(t) = \frac{\gamma G_a L \tau_p}{2 T_a^2} t^2 - \frac{\gamma G_a L \tau_p}{2 T_a} t + \left(1 - \frac{G_a}{G_e} \right) \Omega_0 t. \tag{10}$$

The last term in this phase expression suggests that the sample's NMR spectrum can arise from a FT of the signal, provided that the remaining two terms are accounted for. In fact these two extra phase contributions are not only independent of the Ω_j, but are also given by parameters entirely under our control. We thus propose removing them by multiplying the observed $S(t)$ FID, on a time-by-time basis and at a post-acquisition stage, by their complex conjugates. Starting from Eq. (8), this yields the revised function

$$S'(t) = \exp\left[-\mathrm{i}\left(\frac{\gamma G_a L \tau_p}{2T_a^2}t^2 - \frac{\gamma G_a L \tau_p}{2T_a}t\right)\right]\cdot S(t)$$
$$\propto \sum_j \rho_{\Omega_j}[z_{k(t)}]\exp\left[\mathrm{i}\left(1-\frac{G_a}{G_e}\right)\Omega_j t\right]. \quad (11)$$

Looking for a spectral distribution by Fourier analysis of $S'(t)$ then leads to

$$\mathrm{FT}[S'(t)] \propto \sum_j \int_{\text{time}} \rho_{\Omega_j}[z_{k(t)}]\exp\left[\mathrm{i}\left(1-\frac{G_a}{G_e}\right)\Omega_j t\right]\mathrm{e}^{-\mathrm{i}\omega t}\,\mathrm{d}t$$
$$= \sum_j \int_{\text{time}} \rho_{\Omega_j}[z_{k(t)}]\exp\left[\mathrm{i}\left(\left(1-\frac{G_a}{G_e}\right)\Omega_j - \omega\right)t\right]\mathrm{d}t,$$
$$= \sum_j I(\Omega_j)\cdot\hat{\rho}_{\Omega_j}\otimes\delta\left[\left(1-\frac{G_a}{G_e}\right)\Omega_j - \omega\right]. \quad (12)$$

Eq. (12) clearly reflects the sample's discrete NMR spectrum $I(\Omega)$, with the original frequencies amplified by a known $1-\frac{G_a}{G_e}$ factor and with each peak's point-spread function given by:

$$\hat{\rho}_{\Omega_j} = \int_0^{T_a} \rho_{\Omega_j}[z_{k(t)}]\cdot\mathrm{e}^{-\mathrm{i}\omega t}\,\mathrm{d}t. \quad (13)$$

Given the linear relation between the $z_{k(t)}$ function and t Eq. (9), this means that the peak shapes will be related to the FT of each site's spatial distribution profile (weighted by a hitherto ignored decay that spins may have experienced over a time T_a). In a "best case" scenario $\rho(z)$ will be a well-behaved amplitude-modulated function extending throughout the FOV of interest, thereby supporting a FT over a sizable extent of the $[0, T_a]$ time interval; this would allow us to resolve chemically-shifted sites whenever their frequencies separation $\Delta\nu$ exceeds $(T_a+\tau_p)^{-1}$, akin to what would be observed in conventional spectroscopy. By contrast a "worst case" would comprise an ill-behaved distribution subtending a single Δz spatial voxel, equivalent to a time interval $\Delta t \approx \sqrt{\frac{\gamma G_a L}{T_a}}$ and thereby demanding $\Delta\nu \geqslant \frac{\sqrt{\gamma G_a T_a L}}{T_a+\tau_p}$. Throughout the remainder of this study we shall assume that spatial distributions are smooth and long enough to yield a convolution with well-behaved $\hat{\rho}_{\Omega_j}$ point-spread functions, rather than to a split or an intolerable broadening. With this supposition one can proceed to examine the spatial distribution associated with each Ω_j site simply by filtering the resulting FT$[S'(t)]$ spectrum around a particular chemical shift peak of interest and then recalculating, by inverse FT of its $\hat{\rho}_{\Omega_j}$ peak shape followed by a magnitude calculation, the associated $\rho_{\Omega_j}(z)$ spatial profile. The full sequence of events leading to a spectroscopic imaging correlation by these spatial encoding/decoding means, is summarized for completion in Fig. 2.

2.2. Experimental spectroscopic imaging on a one-dimensional phantom

The preceding arguments were applied to analyze a sample of 99.9% deuterated water (HDO), positioned with a small (≈0.5 ppm) off-resonance offset. Like all remaining experiments in this work this test was carried out at 501 MHz using a high-resolution Varian iNova® NMR spectrometer, equipped with a triple-axis gradient 5 mm probe. The various panels in Fig. 3 illustrate the sequence of events leading then to an effective 2D-type spectroscopic image, starting from the experimental 1D FID. The raw data set $S(t)$ is characterized by a strong phase modulation derived from the quadratic term in Eq. (10). Post-acquisition processing of this signal along the lines of Eq. (11) leads to a $S'(t)$ devoid of strong quadratic modulations, which by FT yields the $I(\Omega)$ sample spectrum. At this point a numerical frequency filtering function can be applied at the Ω_j of interest; then, following an inverse FT and a magnitude calculation, this delivers the associated $\rho_{\Omega j}(z)$ spatial profile.

It is worth focussing on the signal-to-noise ratios (SNRs) that can be expected to characterize, under otherwise identical conditions of spectral/spatial resolution and spectral/spatial bandwidths, the spatially-encoded approach just introduced *vis*-à-*vis* a 2D EPSI-type sequence (Fig. 1b). This comparison needs to account for the different domains and the differing post-acquisition processing procedures that characterize each of the techniques. To make the spectral resolution parameters of both

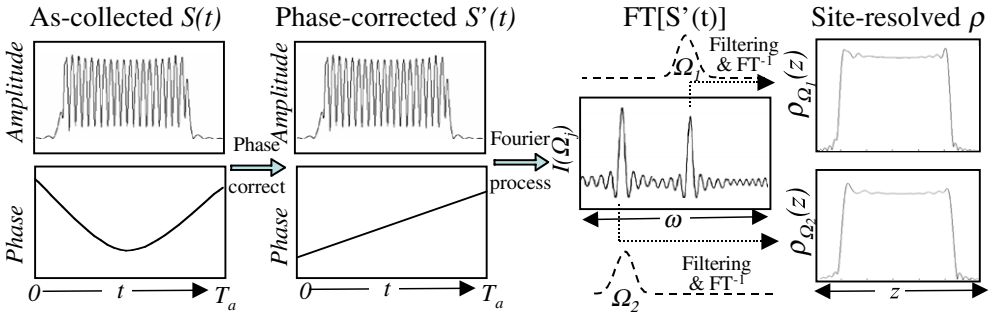

Fig. 2. Summary of events leading to the retrieval of shift-resolved 1D $\rho_\Omega(z)$ images from the FID arising from the spatially-encoded sweep sequence illustrated in Fig. 1c. Steps involve removing $S(t)$'s quadratic phase contribution, FT of the ensuing $S'(t)$ function, filtering out a desired Ω_j component from the resulting NMR spectrum, and inverse-FT this filtered point-spread-function to obtain its originating spatial profile.

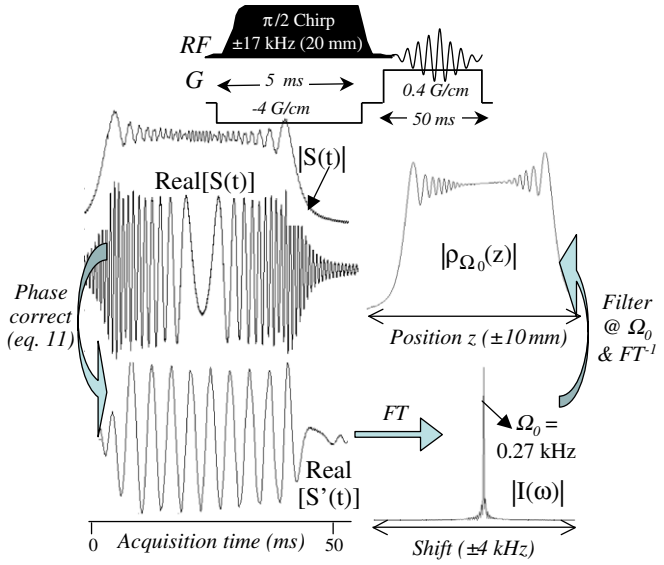

Fig. 3. Experimental illustration of how the pulse scheme shown on top, delivers spectroscopic imaging information from a uniform HDO sample. Signal digitization took place at 10-μs dwells using a 100-kHz receiving filter bandwidth, and the carrier frequency was set slight off-resonance to better illustrate the shift-derived oscillations characterizing the $S'(t)$ signal. The acquisition time used in this experiment, although unnecessarily long for 1D MRI, was chosen in analogy to the read-out dimension time of a 2D single-scan MRI experiment. Notice the sensitivity enhancement occurring upon deriving the spatial profile from the shift-filtered resonance *vis*-à-*vis* the original profile (i.e., $|\rho_{\Omega_0}(z)|$ *vs.* $|S(t)|$), owing to the substantial noise reduction associated to the filtration process.

acquisitions comparable we shall assume that they involve similar total acquisition times T_a, implying that the EPSI imaging stage involves only a $\Delta T_a = T_a/2N$ fraction of this time and uses an acquisition gradient G_a^{EPSI} that is $2N$ times larger than its conventional G_a 1D imaging counterpart. This demand offsets in turn the performance handicap of the spatially-encoded imaging approach, which requires maximum wavenumber values k_{max} that are $\approx N_z = FOV/\Delta z$ times larger than their conventional imaging counterparts for achieving comparable spatial resolutions [23,24]. These larger gradients required by EPSI do not bring a detriment to the overall SNR of the technique, as under ideal conditions this will reflect the summation of images involved upon FT of the data along the spectroscopic encoding axis. Hence, considering as reference a noise defined by a σ_n r.m.s value per-unit of frequency and growing as the square-root of an FOV-defined filter bandwidth, EPSI's SNR can be expressed as

$$SNR^{EPSI} \propto \frac{|\rho_\Omega|\sqrt{N_z}}{\sigma_n\sqrt{\gamma G_a FOV}}, \qquad (14a)$$

where $|\rho_\Omega|$ defines a generic voxel intensity for a particular chemical site, and $\sqrt{N_z}$ reflects the Fellgett advantage inherent to FT-based imaging methods. A main drawback of the spatially-encoded approach is that it will be generally devoid of such multiplex advantage. It can be shown, however, that the FT/filtering/inverse-FT procedure depicted in Fig. 2 equates to re-defining the relevant filter bandwidth as being dictated by a voxel Δz rather than by the full FOV. This leads to a spatially-encoded SNR of

$$SNR^{s\text{-}e} \propto \frac{|\rho_\Omega|}{\sigma_n\sqrt{\gamma G_a^{s\text{-}e}\Delta z}}. \qquad (14b)$$

It follows from these arguments that, SNRwise, both imaging approaches should be comparable. In an effort to test this prediction a number of experiments were run on a mixture containing HDO and dimethylsulfoxide (DMSO), in proportions leading to singlets appearing at ≈4.7 and 2.5 ppm with *ca.* 1.4:1 ratios in their ^{1}H NMR spectrum. Since these two substances are miscible with one another they conform to the "best case" scenario mentioned earlier: a homogeneous solution occupying the entire FOV ($L \approx 18$ mm). This sample was investigated under conditions that, though different, yielded comparable spatial and spectral characteristics for the conventional and spatially-encoded based results. Summaries of the resulting data are shown in Fig. 4. Worth pointing out are the strong amplitude beats appearing in the spatially-encoded $|S(t)|$ signal, coming from interferences between the chemically-shifted resonances, as well as the clear dis-

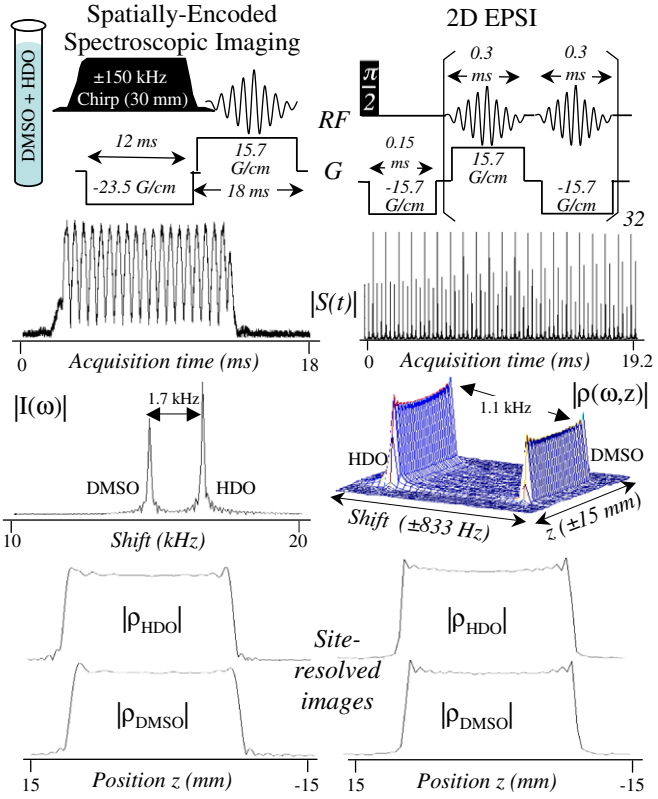

Fig. 4. Comparison of the spectroscopic imaging results that under similar gradient and acquisition conditions, could be extracted using the 1D spatially-encoded imaging and the 2D EPSI sequences from a simple phantom made out of a 5-mm tube containing a HDO/DMSO solution. Both time-domain sets of signals $S(t)$ were digitized at 5-μs dwells using a 300-kHz filter bandwidth. The smaller span of the spatially-encoded signal reflects the fact that only 18-mm out of a 30-mm field-of-view contribute to it; the different peak separations in the two experiments reflects the additional $1 - \frac{G_a}{G_e}$ factor involved in the spatial encoding Eq. (12).

tinction between two chemically inequivalent sites positioned $\approx\delta_{\mathrm{HDO}}-\delta_{\mathrm{DMSO}}=2.2$ ppm apart (approx. 1.7 kHz at 501 MHz when taking the $1-\frac{G_a}{G_e}\approx 1.6$ scaling factor into account), arising from FTing $S(t)$ once this function is freed from its quadratic phase components. Notice that, as expected, the images arising by inverse FT of these clearly resolved sites are then free from the original beats. These results also confirm that sensitivities are comparable for both imaging experiments.

3. Spatially-encoded spectroscopic imaging at higher dimensions

The simplicity underlying the spatially-encoded spectroscopic imaging approach, which is devoid in its 1D spatial version from any multiple fast gradient echoes, proves advantageous when considering its extension to cases with more than one spatial dimension. Different routes allow frequency-swept encoding approaches to monitor multiple spatial dimensions in an "ultrafast" fashion [24], and in fact not all the domains need to be monitored based on these principles. It is sufficient to spatially-encode only one of the spatial axis in order to extract from the resulting experiment the correlated spectroscopic distribution being sought—once again, as in the 1D spatial case treated above, at no additional complexity beyond that involved in the basic imaging pulse sequence. Without attempting a comprehensive treatment we present in this Paragraph one such possibility, relying on the "hybrid" r/k scanning experiment illustrated in Fig. 5. In this experiment spins are initially encoded spatially along the z axis while under the action of G_e^z; subsequently they are incrementally unraveled by a read-out G_a^z gradient, while their distribution along an orthogonal axis is repeatedly imaged in reciprocal space (k_y) via the application of a strong oscillatory gradient G_a^y. Single-scan data collected throughout the course of such pulse sequence can lead to a 2D spatial image if the individual $S(k_y)$ echoes are spliced and 1D FT'd against k_y, correctly positioned within a 2D matrix as a function of the monotonically-rasterized z coordinate, and plotted in magnitude mode (*cf.* Ref. [24], Fig. 5b). Following a reasoning similar to that discussed above, and thanks to the linearity that once again will in this instance relate the physical z and t variables for every coordinate in y (or for every k_y prior to the FT *vs.* k_y), it follows that shift-selective $I(\Omega)$ profiles can become available for different $\rho(y,z)$ simply by performing a post-acquisition processing operation. Indeed, following the definitions given in Fig. 5 and arguments analogous to those leading to Eq. (3) in the 1D case, one can express the encoding phase accrued by the spins prior to the acquisition as the sum of z- and y-dependent functions

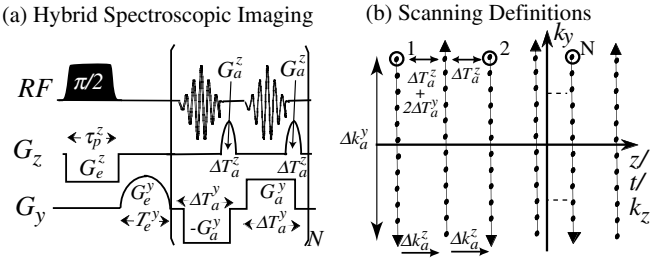

Fig. 5. (a) Example of a single-scan strategy capable of delivering, via its z-axis encoding, the temporal evolution needed to extract 2D images from a correlated spectral dimension. (b) Definition of the various terms used in the text; FT, filtering and inverse FT of the circled data points can be treated as in the 1D case above, to extract the sample's NMR spectrum. Notice that whereas the Δk_a^z (or Δz) increments between points in adjacent frequency-encoded columns are equal (horizontal arrows), their Δt increments are not (horizontal double-arrows). The Cooley–Tukey FT algorithm therefore cannot be applied to jointly process these even and odd elements; on the other hand an interlaced FT [29] would successfully afford a NMR spectrum from such set.

$$\phi_e(z,y)=\underbrace{\left\{\left[-\frac{(\gamma G_e^z)^2\tau_p^z}{2(O_f-O_i)}\right]z^2+\left[\frac{\gamma G_e^z\tau_p^z(O_f-\Omega_0)}{(O_f-O_i)}\right]z^1+\left[\frac{\tau_p^z(2O_f\Omega_0-O_i^2-\Omega_0^2)}{2(O_f-O_i)}\right]z^0\right\}}_{\phi_e^z(z)}+\underbrace{\gamma G_e^y T_e^y}_{\phi_e^y(y)}. \tag{15}$$

During the course of the acquisition the overall spin evolution phase of each particular site becomes

$$\Phi_{\Omega_0}(z,y,t)=\underbrace{\phi_e^z(z)+k_z(t)z}_{\Phi_a^z(z,t)}+\underbrace{\phi_e^y(y)+k_y(t)y}_{\Phi_a^y(y,t)}+\Omega_0 t, \tag{16}$$

and at any given acquisition time t signals will reflect, as before, solely those spins fulfilling the k_z-dependent stationary phase approximation $\frac{\partial}{\partial z}[\Phi_{\Omega_0}(z,y,t)]_{z=z_{k_z(t)}}=0$. Following these arguments, the multi-site observable signal can be written as a 2D analog of Eq. (8):

$$S(t)\propto\sum_{\Omega_j}\exp[\mathrm{i}\Phi_a^z(z_{k_z(t)},t)]\exp[\mathrm{i}\Omega_j t]\cdot\int\rho_{\Omega_j}(z_{k_z(t)},y)\exp[\mathrm{i}\Phi_a^y(y,t)]\,\mathrm{d}y, \tag{17}$$

where the integral incorporates the effects of the k_y-encoding. On considering the z/k_z development at suitable k_y values, such as the $n=1,2,\ldots,N$ points illustrated in Fig. 5b, one can recognize an FID that behaves akin to that treated in the 1D case except for a discretization of the time variable $t_n=t_0+(n-1)\Delta t$, which has now become multiple of $\Delta t=2(\Delta T_a^z+\Delta T_a^y)$. For every k_y value (or every y coordinate deriving from FT against k_y) one can therefore

define a "corrected" spectroscopic FID akin to that derived in Eq. (11):

$$S'(t_n) = \exp\left[-\mathrm{i}\left(\frac{\gamma G_a^z L_z \tau_p^z}{2(\Delta T_a^z)^2} t_n^2 - \frac{\gamma G_a^z L_z \tau_p^z}{2\Delta T_a^z} t_n\right)\right] \cdot S(t_n)$$
$$\propto \sum_{\Omega_j} \exp\left\{\mathrm{i}\left[\left(1 - \frac{G_a^z}{G_e^z}\right)\Delta T_a^z + \Delta T_a^y\right] 2n\Omega_j\right\}$$
$$\cdot \int \rho_{\Omega_j}[z_{k_z(t)}, y] \exp[\mathrm{i}\Phi_a^y(y,t)]\,\mathrm{d}y. \quad (18)$$

Following similar arguments as before, FT of each such signal within the (k_y, k_z) 2D FID affords a spectroscopic characterization of the $I(\Omega_j)$ spectrum which in turn, when appropriately filtered and inverse FT'd, provides the 2D $\rho(z,y)$ image for a particular shift Ω_j.

This data acquisition and filtering procedure was tested once again on a 5-mm diameter NMR tube; this time containing equal volumes of water and of chloroform, with the former deuterated to yield NMR peaks with approximately similar heights. As these compounds maintain separate phases (with the heavier chloroform occupying the lower portion of the tube), the possibility to image their differing positions along the vertical z axis was explored. The protocol just discussed was applied on this mixture, yielding the set of results plotted in Fig. 6. Shown in this Figure underneath the pulse sequence is the time-domain signal arising from this experiment; by contrast to the $|S(t)|$ plots in Fig. 4 these data show, beyond the sharp k_y-driven gradient echoes, only minor interferences along the spatially-encoded axis thanks to the physical separation that now characterizes the two inequivalent sites along this domain. Rearrangement of these data and FT *vs.* the k_y wavenumber yields a 2D $\rho(z,y)$ image that disregards altogether the presence of two inequivalent components. Removing the quadratic phase component in this 2D signal as indicated in Eq. (18) followed by FT along the spatially-encoded direction, gives a shift spectrum which distinguishes between the two chemically inequivalent sites. Filtration of these data in the ω-dimension followed by a return to the spatial domains and magnitude calculation, clearly resolves the 2D profiles occupied by the individual sites (Fig. 6, bottom), affording the shift-resolved imaging information being sought.

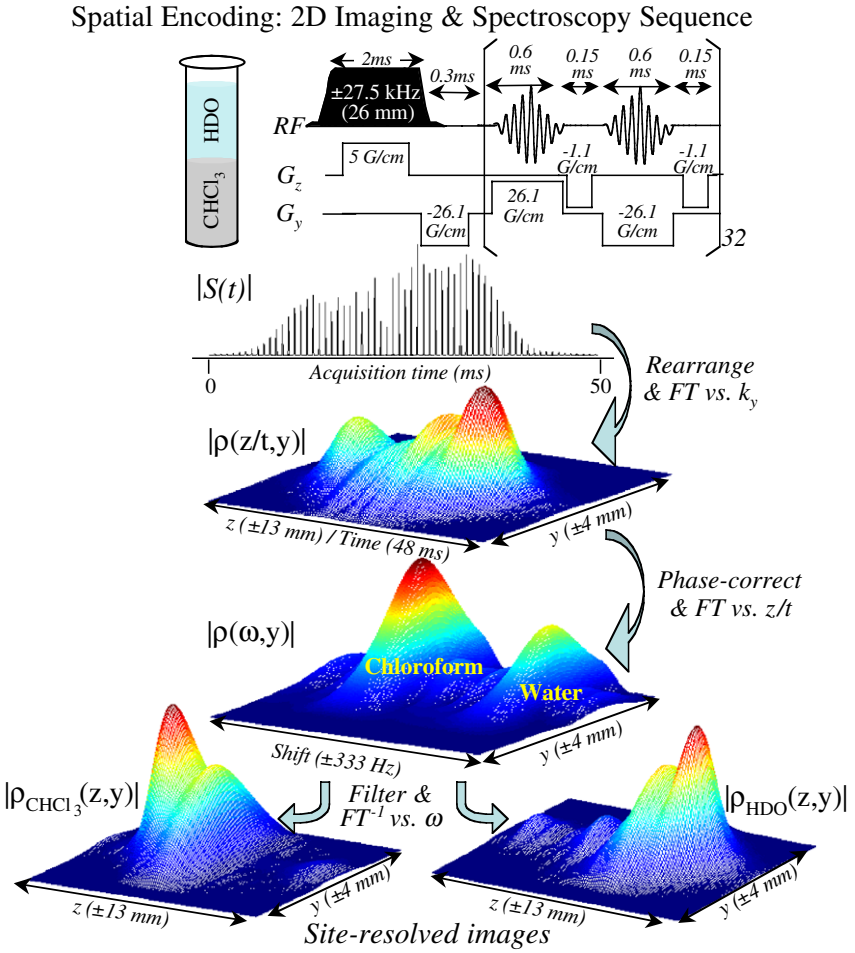

Fig. 6. Results obtained upon applying the single-scan spatial encoding variant illustrated in Fig. 5, towards the acquisition of spectrally-resolved 2D images from a water/$CHCl_3$ 5 mm diameter phantom (top left). Indicated are the sequence parameters used, as well as results arising from various intermediate processing stages; for convenience these employed only odd-value elements in the kz array (even-value elements could be processed similarly and co-added for further improving the SNR). Data in these experiments were digitized throughout the acquisition using a 10-μs dwell and an analog filter bandwidth of 66 kHz (defining an effective 6 mm FOV along y).

The actual pulse sequence needed to retrieve this kind of 1D spectroscopic/2D imaging information is very similar to that underlying a conventional 2D EPI acquisition; in fact the pulse scheme used in Fig. 6 can be transformed into such single-scan imaging sequence simply by replacing the initial frequency-swept $\pi/2$ z-encoding pulse, by a broad-band $\pi/2$ excitation. It is illustrative to explore what kind of 2D images will an EPI sequence afford on the same two-component sample, using very similar timing and gradient-strength conditions as in the spatial encoding case. Fig. 7 shows the resulting image, which highlights the well-known shift/susceptibility distortion of which EPI can suffer—particularly along the low-bandwidth domain. In our case this domain corresponded with the z-axis, which evidences overlapping images between the two sample components due to chemical shift effects.

4. Spatially-encoded single-scan spectroscopic imaging in inhomogeneous fields

4.1. Inhomogeneity compensations disregarding the chemical shift effects

One of the potential strengths of spatial encoding approaches rests in their ability to yield undistorted data in the presence of field inhomogeneities [24,30,31]. We consider next to what extent, if at all, is such ability preserved in the current spectroscopic imaging case. With this as aim, we revert back to a one-dimensional scenario, but with the sample now affected by a $\gamma\Delta B_0(z) = \Omega_{\text{inh}}(z)$ addition to its ideal γB_0 field value, a distortion which we shall assume has been *a priori* mapped and thereby is known. Such field inhomogeneities, if sufficiently large, can naturally ruin the quality of an NMR experiment—regardless of whether this is of an imaging or a spectroscopic nature. The spatially-encoded spectroscopic imaging approach described in the preceding sections is no exception to this rule; Fig. 8 illustrates this by showing the effects that a *ca.* 9-kHz field distribution across the sample will have on the spectrum of a water–DMSO mixture, under acquisition conditions similar to those which yielded the highly resolved peaks in Fig. 4. Driving these distortions is the additional Ω_{inh} term, altering the overall phase of the experiment Eq. (5) as:

$$\Phi_{\Omega_0}(z,t) = \underbrace{\phi_{\text{RF}}[\tau(z)] + [\tau_{\text{p}} - \tau(z)]\cdot[\gamma G_{\text{e}} z + \Omega_0 + \Omega_{\text{inh}}(z)]}_{\phi_{\text{e}}(z)} + k(t)z + \Omega_0 t + \Omega_{\text{inh}}(z)t. \tag{19}$$

The presence of $\Omega_{\text{inh}}(z)$ breaks the linearity between the decoded coordinate z and the acquisition time t; this linearity

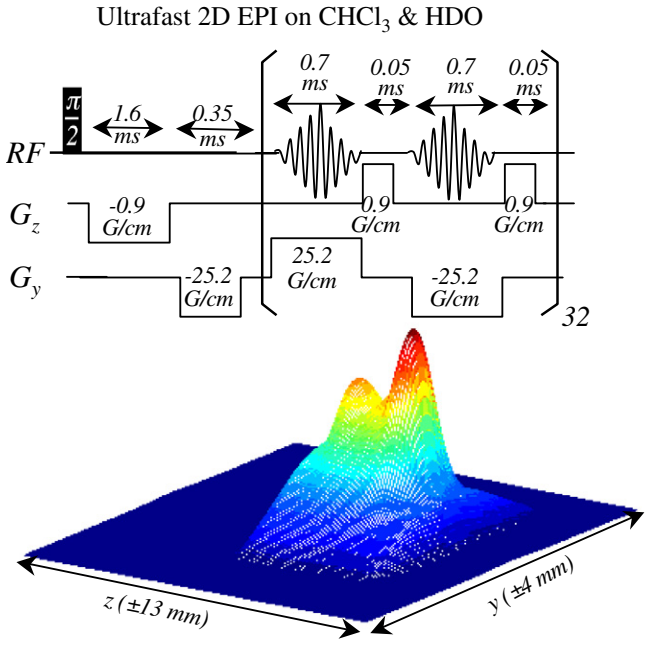

Fig. 7. Experimental results obtained from the same phantom and under similar experimental conditions as those employed in Fig. 6, upon utilizing an echo planar imaging sequence. This sequence differs from that employed in Fig. 6 solely on its reliance on a hard $\pi/2$, instead of on a frequency-swept $\pi/2$ pulse, for the initial excitation (as well as in its data processing aspects). Special attention was paid to repeating the acquisition and gradient settings used in that spectroscopic imaging experiment, including filter bandwidths and digitization rates. Notice that under such conditions not only is the spectroscopic information absent from the EPI data, but also a characteristic artifact shows up along the phase-encoding (z) dimension as a displacement of the off-resonance (in this case the Chloroform) components.

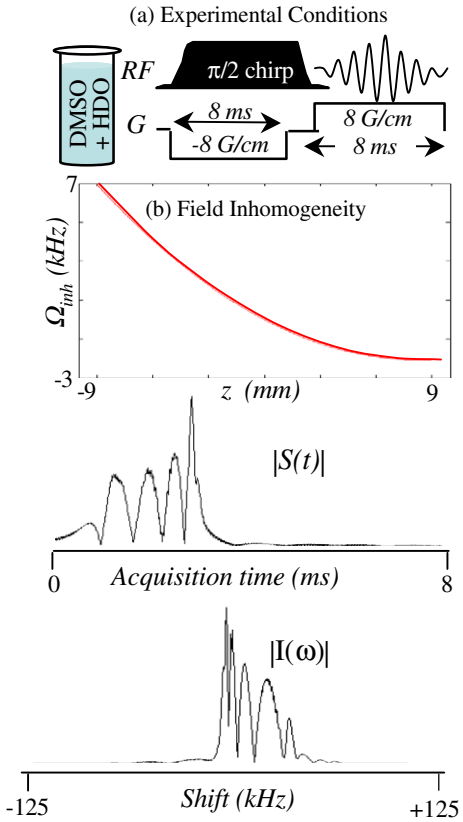

Fig. 8. Spectroscopic and imaging profiles obtained under conditions (a), similar to those detailed in Fig. 4, but under the effects of the z-dependent field inhomogeneity illustrated in (b). Given the absence of identifiable chemical resonances in $I(\omega)$, the retrieval of site-resolved $\rho_\Omega(z)$ profiles cannot be attempted.

conformed an important ingredient underlying our image-retrieval procedure, and was an essential requirement for the extraction of a chemical shift spectrum by FT of the data against z/t. In addition to these problems $\Omega_{\mathrm{inh}}(z)$ will affect voxel sizes Δz throughout the acquisition process, bringing about an image distortion and a rapid decay of the $S(t)$ signal.

And yet, as detailed elsewhere for a chemical-shift-free scenario [24], the fact that $\Omega_{\mathrm{inh}}(z)$ has been mapped enables spatial encoding to carry out a voxel-by-voxel experimental compensation of the inhomogeneities, and thereby a restoration of the image's faithfulness. Two variables were exploited in Ref. [24] to perform such correction: the local phase profile $\phi_{\mathrm{RF}}(z)$ imparted by the frequency-swept RF during the course of the excitation, and the strength of the acquisition gradient $G_{\mathrm{a}}(t)$ governing the time required by each of the excited voxels for undergoing refocusing. Chemical shifts, however, will prevent this kind of precise manipulations, as the relation between the manipulating offset and the z positions will now be distorted by the presence of an unknown shift Ω_0. This uncertainty will in general complicate the correction of field inhomogeneities by gradient- or RF-based manipulations. Still, we considered it worth exploring what kind of performance will the compensation method described in Ref. [24] yield when applied in combination with the spectroscopic imaging processing introduced in Section 2—even if disregarding the effects of chemical shifts altogether. Denoting the relevant parameters for this $\Omega_0 = 0$ case by overbar templates, we then have

$$\Phi_{\Omega_0=0}(z,t) = \overline{\Phi}(\bar{z},t) = \overline{\phi}_{\mathrm{e}}(\bar{z}) + k(t)\bar{z} + \Omega_{\mathrm{inh}}(\bar{z})t. \tag{20}$$

For such on-resonance situation we briefly remind that the Ω_{inh} compensation approach could be cast by demanding

$$\text{(i)}\ \frac{\mathrm{d}}{\mathrm{d}t}\left[\frac{\mathrm{d}^2\bar{\Phi}(z,t)}{\mathrm{d}z^2}\right]_{z=\bar{z}_{k(t)}} = 0 \tag{21a}$$

which ensures a constant pixel resolution throughout the course of the acquisition, and

$$\text{(ii)}\ \gamma\overline{G_{\mathrm{a}}}(t) = \left\{-\frac{\mathrm{d}}{\mathrm{d}t}\left[\frac{\mathrm{d}\overline{\phi_{\mathrm{e}}}(z)}{\mathrm{d}z}\right] - t\cdot\frac{\mathrm{d}}{\mathrm{d}t}\left[\frac{\mathrm{d}\Omega_{\mathrm{inh}}(z)}{\mathrm{d}z}\right] - \frac{\mathrm{d}\Omega_{inh}(z)}{\mathrm{d}z}\right\}_{z=\bar{z}_{k(t)}} \tag{21b}$$

which incorporates the demand for a linear spatial/decoding-time relation $\bar{z}_{k(t)} = \frac{L}{2} - \frac{L}{T_{\mathrm{a}}}\cdot t$. Fig. 9 presents two sets of results acquired upon including these corrections in our new spectroscopic imaging experiments, involving the same sample and inhomogeneity parameters as those leading to the highly distorted data shown in Fig. 8. The success of the compensation procedure imparted by Eqs. 21 is clearly illustrated by the long ensuing $S(t)$ FIDs, by the good degree of separation between the chemical sites that can now be resolved, and by the undistorted $\rho(z)$ images that these data can afford upon being subject to the procedure summarized in Fig. 2.

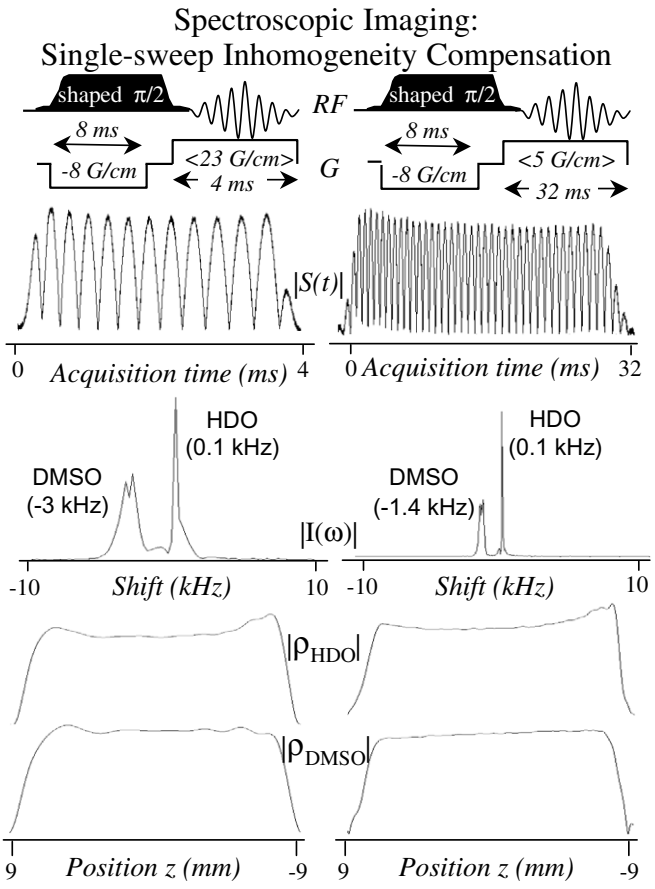

Fig. 9. Experimental application of the field-compensating principles described in Ref. [24], to the spectroscopic imaging approach described in the present work. Data were collected under the various indicated conditions, using RF pulses and acquisition gradients shaped according to Eq. (21) and the field inhomogeneity profile depicted in Fig. 8. As a result of the correction both the spectroscopic as well as the site-resolved imaging capabilities of the method are restored, even if the shaping of the RF and of $G_{\mathrm{a}}(t)$ prevent us from describing the chemical shift scaling by a simple $1 - \frac{G_{\mathrm{a}}}{G_{\mathrm{s}}}$ factor. Notice the larger residual broadening of the off-resonance (DMSO) signal.

4.2. Offset-balanced inhomogeneity compensation

These considerations notwithstanding, a closer look at the spectra in Fig. 9 confirms that the quality of the correction is not the same for all sites: the water peak appearing near the on-resonance condition displays an excellent Ω_{inh} compensation, whereas the DMSO peak at $\Omega_0 \approx 1.5$ kHz shows a residual inhomogeneity-driven broadening. This offset dependence reflects the $\delta z = \Omega_0/\gamma G$ errors introduced by chemical shifts during the course of the RF compensation and subsequent G_{a}-driven decoding. Understanding the exact form of these effects opens new avenues for their compensation; the present paragraph is devoted to this topic.

We should begin by noting that a spectroscopic imaging approach of the kind introduced in Section 2 but incorporating a complete compensation of all offset-driven artifacts for arbitrary chemical shift values, seems *a priori* unlikely. The reason for this lies in the fact that, as detailed

in Ref. [24], inhomogeneities transform the Φ function into a higher-order (>2nd degree) z polynomial. In the chemical shift case this translates into a high-order δz—or in other words into a high-order Ω_0—phase function; reverting such acquisition phase into the linear expression needed by a FT treatment (Eq. (11)) does not appear in general viable. Still, it is enlightening to compute what kind of phase distortions will the presence of small chemical offsets introduce; i.e., what kind of changes will be introduced in Φ's expression to first order in Ω_0 and (equivalently) in δz. Using as starting point the phase expression Eq. (19) and the overbar $z(t) = \bar{z}(t) + \delta z$ notation introduced in Eq. (20), a Taylor expansion of $\Phi_{\Omega_0}(z,t)$ can be made as

$$\begin{aligned}\Phi_{\Omega_0}(z,t) &= \overline{\Phi}(\bar{z},t) + \underbrace{\left(\frac{\partial \overline{\Phi}_{\Omega_0=0}}{\partial z}\right)_{z=\bar{z}_{k(t)}}}_{0}\delta z \\ &\quad + \left(\frac{\partial \Phi}{\partial \Omega_0}\right)_{\substack{\Omega_0=0 \\ z=\bar{z}_{k(t)}}}\Omega_0 \\ &= \overline{\Phi}(\bar{z},t) + \left[\left(\frac{\partial \phi_e}{\partial \Omega_0}\right)_{\substack{\Omega_0=0 \\ z=\bar{z}_{k(t)}}} + t\right]\Omega_0.\end{aligned} \tag{22}$$

Here we have set $\left(\frac{\partial \overline{\Phi}_{\Omega_0=0}}{\partial z}\right)$ to zero as this is fulfilled by all $\bar{z}_{k(t)}$ voxels conforming to the stationary phase condition, and have only considered terms proportional to δz and Ω_0 thereby disregarding all terms of order $O(\Omega_0^2, \Omega_0 \delta z, \delta z^2)$ and higher. Eq. (22) is revealing because it indicates that, were it not for the encoding-phase chemical-shift dependence embodied by $\left(\frac{\partial \phi_e}{\partial \Omega_0}\right)$, one would obtain an ideal shift-free phase expression plus a simple $\Omega_0 t$ term derived from the acquisition portion of the experiment—which is in turn the "high resolution" term being sought to extract spectroscopic information from the data. This means that, at least to first order, one would face no complications in achieving inhomogeneity compensations balanced with respect to chemical shift offsets, if one were to rely on encoding phases ϕ_e profiles that are fully devoid of Ω_0 effects.

With this clue in hand we propose a more efficient, shift-independent inhomogeneity compensation sequence, based on imparting an initial encoding phase that is independent of Ω_0 and solely dependent on gradient-derived effects. In an ideal shift- and inhomogeneity-free case such phase would be simply proportional to z^2 (Eq. (3) with $\Omega_0 = 0$), which is the basic profile demanded by spatially-encoded imaging. This requirement is reminiscent of—but in fact opposite to—the encoding demands posed by single-scan 2D NMR spectroscopy: there one requests that the initial encoding phase be made dependent on Ω_0 shifts, but devoid of quadratic gradient effects [21]. Numerous continuous alternatives exist for achieving such aim; all of these based on the application of two consecutive frequency-swept pulses acting under the effects of different gradients [32–35]. For the present case, we chose to focus on the $\pi/2$–π pulse combination, involving the application of two frequency-swept pulses whose amplitudes have been tuned to impart an initial excitation and a subsequent inversion of all spins passing through their resonance. In the different 2D NMR alternatives discussed for this sequence [34,35], the two gradients and the sense of the RF sweeps were chosen so as to make the first sample element to be excited also the element that undergoes first the gradient's refocusing. This allows one to generate an encoding phase that, while linear in z and Ω_0, is devoid of quadratic gradient-derived effects. By contrast our focus here is on a sequence where $\pi/2$ and π pulses address voxels in the opposite manner; eliminating the $z{\cdot}\Omega_0$ effects, and leaving at their conclusion solely higher-order, gradient-derived encoding terms. A compact description of how the RF pulses and gradient shapes required for executing this new kind of $\pi/2$–π inhomogeneity compensation scheme can be computed, is summarized for convenience in the Appendix. Fig. 10 summarizes some of the results arising from the ensuing pulse sequence, upon applying it to correct the same kind of inhomogeneities distorting the data in Fig. 8. As can be appreciated from this summary the new sequence can successfully deliver its spectroscopic imaging profiles free from inhomogeneity distortions; comparison of these data against the results shown in Fig. 9 also evidences the superiority of the $\pi/2$–π dual-sweep encoding over its simpler $\pi/2$ single-sweep counterpart, to compensate for the effects of chemical shifts. Numerical calculations (not shown) show that this new sequence can compensate field inhomogeneities through a wide span of ^{1}H-relevant shifts; a compensation evidenced by both sharper resonances in the

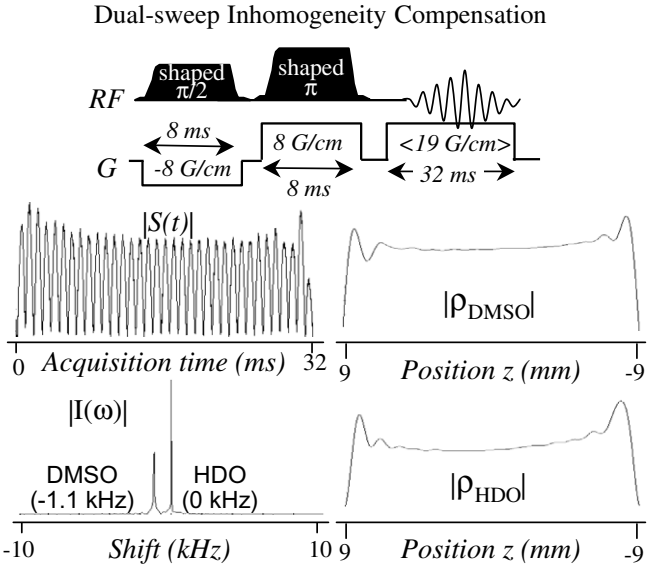

Fig. 10. Experimental demonstration of the broadband field-compensating abilities arising upon extending the single-sweep principles described in Ref. [24], to a dual-sweep experiment removing to first order all the chemical shift effects from the initial encoding phase. While the processing of these data is as in Fig. 9, notice the sharpness characterizing now the off-resonance DMSO peak. The principles of the method are further detailed in the text and Appendix.

spectral domain as well as by less distorted images in the spatial one.

5. Discussion and conclusions

A few years ago we demonstrated that the encoding underlying ultrafast 2D NMR, yields spectral peak shapes that enable the extraction of spatial information at no extra complexity in the experiment's performance [36]. It was then shown that, provided sufficient spectral resolution exists between peaks along the indirect domain and that their spatially-encoded distributions are sufficiently well behaved, the gradient-based unraveling of the indirect-domain frequencies enables one to locate the spins' spatial positions by FT of their peaks' echo shapes. In a somewhat complementary manner, the present study shows that spectroscopic information lies along the imaging domain of the spatially-encoded ultrafast MRI experiment. Once again, no complication beyond the execution of the basic imaging experiment is necessary for extracting such spectral information. And also in this case, spectra arise by FT of a domain that hitherto remained untransformed, and thereby contained a certain degree of underutilized information. In further analogy to the ultrafast 2D NMR case, extraction of spectral data from the imaging profiles will again be conditioned by the interplay between the site resolution being sought, and the spatial distribution supporting the point-spread functions of the spectral lineshapes. In the model cases that were here described these functions were well behaved, as they arose from homogeneous distributions. It remains to be seen what kind of performance is observed in realistic *in vivo* experiments; tests of this kind are currently in progress.

These caveats aside, it appears that a number of attractive features are associated with the spectroscopic imaging approach that was here described. In terms of implementation the spatially-encoded pulse sequences are simpler than their 2D EPSI counterpart, as their data acquisition "saves" the experiment of a fast-oscillating gradient-echo train. This may not be crucial when attempting to monitor a single spatial dimension, but becomes important upon extending the method to higher dimensionalities requiring an increasing number of nested gradient oscillations. It may be worth pointing out that in this latter case spatial encoding approaches may also be designed so as to provide identically large spectroscopic spectral bandwidths, regardless of the number of dimensions involved. On the other hand it is also clear that the train of oscillating gradients is what provides EPSI with its generality, and absence of demands with regards to the spatial distributions that the chemicals being analyzed need to adopt. From a technical standpoint, the simplifications introduced by the spatially-encoded acquisition over the EPSI approach are in fact reminiscent of those arising from BURST-derived spectroscopic imaging methods [37,38], whose image-readout portions are also executed under a constant acquisition gradients. Yet by contrast to DANTE-based multi-echo experiments [39] our new proposal is designed to use all spins in the sample; this has a positive impact in the SNR observed for the resulting images, and even further performance gains can be expected when operating in slower gradient switching systems such as those typical of wide-bore MRI scanners.

A final feature worth highlighting concerns the compatibility of the new spectroscopic imaging approach here presented, with the inhomogeneity compensation methods recently illustrated for the spatial encoding imaging approach in a shift-free scenario. These advantages were brought to bear using the original single-sweep encoding sequence and found effective if the chemical shift offsets were small; i.e., if inhomogeneities $\Omega_{\mathrm{inh}}(z)$ changed by less than a radian within a $\delta z = \Omega_0/\gamma G_{\mathrm{e}}$ interval. More sophisticated options were also derived to take care of larger displacements—at least up to second order in δz. These features could find use in the analysis of realistic problems; tests on the potential of these different pulse sequences are currently in progress on *in vivo* systems.

Acknowledgments

This work was supported by the Israel Science Foundation (ISF 1206/05) and by the Horowitz Fund (Project 531). A.T. acknowledges the Clore Foundation for a Ph.D. fellowship.

Appendix

The actual details of how to compute the RF pulses and the gradient shapes required for programming the new $\pi/2$–π inhomogeneity compensation sequence introduced in Section 4.2, are analogous to those given in Ref. [24] for the case of a single RF pulse sweep albeit modified by shift effects according to the Ω_0-expansion arguments in Section 4.2. Briefly, this correction starts from a suitable revision of Eqs. (1)–(3) so as to deal with consecutive $\pi/2$–π encoding pulses:

$$\phi_{\mathrm{e}}(z) = \phi_{\mathrm{e}}^{(\pi)}(z) - \phi_{\mathrm{e}}^{(\pi/2)}(z), \tag{A.1}$$

with

$$\phi_{\mathrm{e}}^{(\pi/2)}(z) = \phi_{\mathrm{RF}}^{(\pi/2)}(z) + \left[\tau_{\mathrm{p}}^{(\pi/2)} - \tau^{(\pi/2)}(z)\right] \cdot \left[\gamma G_{\mathrm{e}}^{(\pi/2)} z + \Omega_0 + \Omega_{\mathrm{inh}}(z)\right] \tag{A.2}$$

and

$$\phi_{\mathrm{e}}^{(\pi)}(z) = 2\phi_{\mathrm{RF}}^{(\pi)}(z) + \left[\tau_{\mathrm{p}}^{(\pi)} - 2\tau^{(\pi)}(z)\right] \cdot \left[\gamma G_{\mathrm{e}}^{(\pi)} z + \Omega_0 + \Omega_{\mathrm{inh}}(z)\right]. \tag{A.3}$$

To account then for the effects of chemical shifts up to first order we rely on the series expansion Eq. (22); following this expression and Eqs. (A.1)–(A.3), these will be given by

$$\Phi_{\Omega_0}(z,t) \approx \overline{\Phi}(\bar{z},t) + \left[(\tau_{\mathrm{p}}^{(\pi)} - \tau_{\mathrm{p}}^{(\pi/2)}) + (\tau^{(\pi/2)}(\bar{z}) - 2\tau^{(\pi)}(\bar{z})) + t\right]\Omega_0. \tag{A.4}$$

As in the single-sweep case, we eliminate now the effects of inhomogeneities by designing $\phi_{\mathrm{e}}(\bar{z})$ and $G_{\mathrm{a}}(t)$ functions so that Eqs. (21), as applied on $\overline{\Phi}(\bar{z},t)$, are fulfilled. The reliance on *two* independent $\pi/2$ and π sweeps gives now extra freedom to arrive to the desired $\phi_{\mathrm{e}}(\bar{z})$ expression; we exploit this in order to reinstate ideality into the spectroscopic component of the phase Φ_{Ω_0}, by making the extra $\tau^{(\pi/2)}(\bar{z}) - 2\tau^{(\pi)}(\bar{z})$ term modulating chemical shifts in Eq. (A.4) linear in t—or equivalently, linear in $\bar{z}$. This will ensure that the compensation neither adds nor detracts from the spectroscopic performance of the measurement. Using arguments akin to those leading to Eq. (39) in Ref. [24], the timings of the RF pulses characterizing these two sweeps will therefore have to fulfill

$$\begin{aligned}\tau^{(\pi/2)}(\bar{z}) &= \tau_{\mathrm{p}}^{(\pi/2)} - \frac{\frac{\mathrm{d}\phi_{\mathrm{e}}^{(\pi/2)}}{\mathrm{d}\bar{z}}}{\left[\gamma G_{\mathrm{e}}^{(\pi/2)} + \frac{\mathrm{d}\Omega_{\mathrm{inh}}}{\mathrm{d}\bar{z}}\right]},\\ 2\tau^{(\pi)}(\bar{z}) &= \tau_{\mathrm{p}}^{(\pi)} - \frac{\frac{\mathrm{d}\phi_{\mathrm{e}}^{(\pi)}}{\mathrm{d}\bar{z}}}{\left[\gamma G_{\mathrm{e}}^{(\pi)} + \frac{\mathrm{d}\Omega_{inh}}{\mathrm{d}\bar{z}}\right]},\end{aligned} \tag{A.5}$$

subject to the opposing-sweeps boundary conditions

$$\tau^{(\pi/2)}\left(\bar{z}_i^{(\pi/2)} = -L/2\right) = 0, \quad \tau^{(\pi/2)}\left(\bar{z}_f^{(\pi/2)} = L/2\right) = \tau_{\mathrm{p}}^{(\pi/2)}, \tag{A.6}$$

$$\tau^{(\pi)}\left(\bar{z}_i^{(\pi)} = L/2\right) = 0, \qquad \tau^{(\pi)}\left(\bar{z}_f^{(\pi)} = -L/2\right) = \tau_{\mathrm{p}}^{(\pi)}.$$

These expressions define the ratio between the sweep times of the two pulses

$$\frac{\tau_{\mathrm{p}}^{(\pi/2)}}{\tau_{\mathrm{p}}^{(\pi)}} = -\frac{\gamma G_{\mathrm{e}}^{(\pi)} + \frac{\mathrm{d}\Omega_{\mathrm{inh}}}{\mathrm{d}\bar{z}}\big)_{\bar{z}=L/2}}{\gamma G_{\mathrm{e}}^{(\pi/2)} + \frac{\mathrm{d}\Omega_{\mathrm{inh}}}{\mathrm{d}\bar{z}}\big)_{\bar{z}=-L/2}}, \tag{A.7}$$

where we allow for a "negative time" definition as involving a regular sweep time but with a reversed sweep rate, to suit the gradient signs that were chosen. These equations, when merged with the above-mentioned $\tau^{(\pi/2)}(\bar{z}) - 2\tau^{(\pi)}(\bar{z}) \stackrel{!}{=} a + b\cdot\bar{z}$ demand, lead to a system of two coupled equations with two unknowns. In the easily achievable $G_{\mathrm{e}}^{(\pi/2)} - G_{\mathrm{e}}^{(\pi)} \neq 0$ case, these can be solved to yield the expressions needed for computing the RF pulse shapes:

$$\begin{cases}\frac{\mathrm{d}\ phi_{\mathrm{e}}^{(\pi/2)}}{\mathrm{d}\bar{z}} = \left[\gamma G_{\mathrm{e}}^{(\pi/2)} + \frac{\mathrm{d}\Omega_{\mathrm{inh}}}{\mathrm{d}\bar{z}}\right]\left\{\frac{Q - \left[\gamma G_{\mathrm{e}}^{(\pi)} + \frac{\mathrm{d}\Omega_{\mathrm{inh}}}{\mathrm{d}\bar{z}}\right]Z}{\left[\gamma G_{\mathrm{e}}^{(\pi)} - \gamma G_{\mathrm{e}}^{(\pi/2)}\right]}\right\}\\ \frac{\mathrm{d}\phi_{\mathrm{e}}^{(\pi)}}{\mathrm{d}\bar{z}} = \left[\gamma G_{\mathrm{e}}^{(\pi)} + \frac{\mathrm{d}\Omega_{\mathrm{inh}}}{\mathrm{d}\bar{z}}\right]\left\{\frac{Q - \left[\gamma G_{\mathrm{e}}^{(\pi/2)} + \frac{\mathrm{d}\Omega_{\mathrm{inh}}}{\mathrm{d}\bar{z}}\right]Z}{\left[\gamma G_{\mathrm{e}}^{(\pi)} - \gamma G_{\mathrm{e}}^{(\pi/2)}\right]}\right\}\end{cases} \tag{A.8}$$

with Q and Z two $\bar{z}$-dependent functions

$$Q \equiv \frac{2\pi(\bar{z}+L/2)}{(\Delta z)^2} - t\frac{\mathrm{d}\Omega_{inh}}{\mathrm{d}\bar{z}} + \frac{T_{\mathrm{a}}}{L}\left[\Omega_{\mathrm{inh}}(\bar{z}) - \Omega_{\mathrm{inh}}\left(-\frac{L}{2}\right)\right] \tag{A.9}$$

$$Z \equiv \frac{-\tau_{\mathrm{p}}^{(\pi/2)}}{2} + \frac{2\tau_{\mathrm{p}}^{(\pi)} + \tau_{\mathrm{p}}^{(\pi/2)}}{L}\bar{z}.$$

The computation of the actual RF shapes follows from here with arguments that are analogous to those given in Ref. [24]: the phase derivatives from Eq. (A.8) are inserted in Eq. (A.5) to derive the $\tau(\bar{z})$ sweep conditions for each of the pulses; these are then reversed into $\bar{z}(\tau)$ functions, and inserted into algorithms that based on the $\mathrm{O}(\tau) = \gamma G_{\mathrm{e}}\bar{z}(\tau) + \Omega_{\mathrm{inh}}[\bar{z}(\tau)]$ offset expression compute the instantaneous phase and amplitude of each pulse during the course of the sweeps. It was on the basis of these calculations that the highly compensated results shown in Fig. 10, were obtained.

References

[1] P.T. Callaghan, Principles of Nuclear Magnetic Resonance Microscopy, Oxford University Press, Oxford, 1991.
[2] M. Levitt, Spin Dynamics, John Wiley and Sons, New York, 2001.
[3] M.A. Bernstein, K.F. King, X.J. Zhou, Handbook of MRI Pulse Sequences, Academic Press, San Diego, 2004.
[4] P. Mansfield, P.K. Grannel, NMR diffraction in solids? J. Phys. C: Solid State Phys. 6 (1973) L422–L426.
[5] P.C. Lauterbur, Image formation by induced local interactions: examples employing nuclear magnetic resonance, Nature 242 (1973) 190–191.
[6] W.P. Aue, E. Bartholdi, R.R. Ernst, Two dimensional spectroscopy: application to nuclear magnetic resonance, J. Chem. Phys. 64 (1976) 2229–2246.
[7] T.R. Brown, B.M. Kincaid, K. Ugurbil, NMR chemical shift imaging in three dimensions, Proc. Natl. Acad. Sci. USA 79 (1982) 3523–3526.
[8] W.T. Dixon, Simple proton spectroscopic imaging, Radiology 153 (1984) 189–194.
[9] J.H. Duijn, G.B. Matson, A.A. Maudsley, M.W. Weiner, 3D phase encoding 1H spectroscopic imaging of human brain, Magn. Reson. Imaging 10 (1992) 315–319.
[10] C.T.W. Moonen, G. Sobering, P.C.M. Van Zijl, J. Gillen, M. von Kienlin, A. Bizzi, Proton spectroscopic imaging of human brain, J. Magn. Reson. 98 (1992) 556–575.
[11] J.P. Cousins, Clinical MR spectroscopy: fundamentals, current applications, and future potential, Am. J. Radiol. 164 (1995) 1337–1347.
[12] D.B. Vigneron, J. Kurhanewicz, S.J. Nelson, Proton chemical shift imaging in cancer, in: C.B. Higgins, H. Hricak, C.A. Helms (Eds.), Magnetic Resonance Imaging of the Body, Raven Press, New York, 1997.
[13] R. Katz-Brull, P.T. Lavin, R.E. Lenkinski, Clinical utility of proton magnetic resonance spectroscopy in characterizing breast lesions, J. Natl. Cancer Inst. 94 (2002) 1197–1203.
[14] P.B. Barker, D.D.M. Lin, In vivo proton MR spectroscopy of human brain, Prog. Nucl. Magn. Reson. Spectrosc. 49 (2006) 99–128.
[15] R. Pohmann, M. von Kienlin, A. Haase, Theoretical evaluation and comparison of fast chemical shift imaging methods, J. Magn. Reson. 129 (1997) 145–160.
[16] R.V. Mulkern, L.P. Panych, Echo planar spectroscopic imaging, Concepts Magn. Reson. 13 (2001) 213–237.
[17] P. Mansfield, Multi-planar image formation using NMR spin echoes, J. Phys. C: Solid State Phys. 10 (1977) 55–58.
[18] P. Mansfield, Spatial mapping of the chemical shift in NMR, Magn. Reson. Med. 1 (1984) 370–386.
[19] D.B. Twieg, The k-trajectory formulation of the NMR imaging process with applications in analysis and synthesis of imaging methods, Med. Phys. 10 (1983) 610–621.
[20] F. Schmidt, M.K. Stehling, R. Turner, Echo Planar Imaging: Theory, Technique and Application, Springer Verlag, Berlin, 1998.
[21] L. Frydman, T. Scherf, A. Lupulescu, The acquisition of multidimensional NMR spectra within a single scan, Proc. Natl. Acad. Sci USA 99 (2002) 15858–15862.

[22] L. Frydman, T. Scherf, A. Lupulescu, Principles and features of single-scan two-dimensional NMR spectroscopy, J. Am. Chem. Soc. 125 (2003) 9204–9217.
[23] Y. Shrot, L. Frydman, Spatially-encoded NMR and the acquisition of 2D magnetic resonance images within a single scan, J. Magn. Reson. 172 (2005) 179–190.
[24] A. Tal, L. Frydman, Spatial encoding and the acquisition of high definition MR images in inhomogeneous magnetic fields, J. Magn. Reson. 182 (2006) 179–194.
[25] D. Kunz, Use of frequency-modulated RF pulses in MR imaging experiments, Magn. Reson. Med. 3 (1986) 377–384.
[26] D. Kunz, Frequency-modulated RF pulses in spin-echo and stimulated-echo experiments, Magn. Reson. Med. 4 (1987) 129–136.
[27] J.G. Pipe, Spatial encoding and reconstruction in MRI with quadratic phase profiles, Magn. Reson. Med. 33 (1995) 24–33.
[28] J.G. Pipe, Analysis of localized quadratic encoding and reconstruction, Magn. Reson. Med. 36 (1996) 137–146.
[29] R.N. Bracewell, The Fourier Transform and Its Applications, McGraw-Hill, New York, 1978, Chapter 10.
[30] B. Shapira, L. Frydman, Spatial encoding and the acquisition of high-resolution NMR spectra in inhomogeneous magnetic fields, J. Am. Chem. Soc. 126 (2004) 7184–7185.
[31] D. Topgaard, R.W. Martin, D. Sakellariou, C.A. Meriles, A. Pines, "Shim pulses" for NMR spectroscopy and imaging, Proc. Natl. Acad. Sci. USA 101 (2004) 17576–17581.
[32] Y. Shrot, B. Shapira, L. Frydman, Ultrafast 2D NMR spectroscopy using a continuous spatial encoding of the spin interactions, J. Magn. Reson. 171 (2004) 162–169.
[33] P. Pelupessy, Adiabatic single-scan 2D NMR spectroscopy, J. Am. Chem. Soc. 125 (2003) 12345–12351.
[34] A. Tal, B. Shapira, L. Frydman, A continuous phase-modulated approach to spatial encoding in ultrafast 2D NMR spectroscopy, J. Magn. Reson. 176 (2005) 107–114.
[35] N.S. Andersen, W. Kockenberger, A simple approach for phase-modulated single-scan 2D NMR spectroscopy, Magn. Reson. Chem. 43 (2005) 795–797.
[36] Y. Shrot, L. Frydman, Spatially-resolved multidimensional NMR spectroscopy within a single scan, J. Magn. Reson. 167 (2004) 42–48.
[37] P.M. Jakob, A. Ziegler, S.J. Doran, M. Decorps, Echo-time-encoded burst imaging (EBI): a novel technique for spectroscopic imaging, Magn. Reson. Med. 33 (1995) 573–578.
[38] P.M. Jakob, F. Kober, R. Pohmann, A. Haase, Single-shot spectroscopic imaging (SISSI) using a PEEP/BURST hybrid, J. Magn. Reson. B 110 (1996) 278–283.
[39] I.J. Lowe, R.B. Wysong, DANTE ultrafast imaging sequence (DUFIS), J. Magn. Reson. B 101 (1993) 106–109.